INTERNATIONAL JOURNAL FOR NUMERICAL METHODS IN FLUIDS
Int. J. Numer. Meth. Fluids 2000; **34**: 187–205

Computational fluid flow in two dimensions using simple T4/C3 element

Y. J. Jan[a,*,1], S. J. Huang[b] and T. Y. Lee[b]

[a] *Department of Marine Engineering, National Kao-Hsiung Institute of Marine Technology, Kao-Hsiung, 811 Taiwan*
[b] *Department of Chemical Engineering, National Tsing Hua University, Hsin-Chu, 300 Taiwan*

SUMMARY

The application of the four nodes for velocity and three nodes for pressure (T4/C3) element discretization technique for simulating two-dimensional steady and transitional flows is presented. The newly developed code has been validated by the application to three benchmark test cases: driven cavity flow, flow over a backward-facing step, and confined surface rib flow. In addition, a transitional flow with vortex shedding has been studied. The numerical results have shown excellent agreement with experimental results, as well as with those of other simulations. It should be pointed out that the advantages of the T4/C3 finite element over other higher-order elements lie in its computational simplicity, efficiency, and less computer memory requirement. Copyright © 2000 John Wiley & Sons, Ltd.

KEY WORDS: T4/C3 element; transitional vortex shedding

1. INTRODUCTION

The finite element simulations of various flow problems using higher-order elements, such as the eight nodes for velocity and four nodes for pressure (Q8/C4 element [1]), Q9/C4 element [2], and T6/C3 element [2], have been widely tested. The effort associated with these higher-order elements mainly resides in the integration of the integrand through complex finite element formulations. Furthermore, the degrees of freedom for these higher-order elements, such as Q9/C4, having 22 variables more than that of T4/C3 [3], which is 11 degrees of freedom, consume more computational resources. However, the use of the simple three nodes for pressures and four nodes for velocities (T4/C3) in flow simulations has not been investigated extensively.

In this paper, we would like to present a detailed T4/C3 finite element formulation in two-dimensional flow simulation, with the developed code validated by three test cases for steady state and a case for transitional flow in vortex shedding. The chosen test cases for the

* Correspondence to: PO Box 8-30, Hsin-Chu City, Taiwan.
[1] E-mail: yjjan@mail.nkimt.edu.tw

Received April 1997
Revised September 1997

steady state are driven cavity flow, flow over a backward-facing step, and confined surface rib flow.

Recently, vortex meters to measure the flow rate have been studied and applied to various industrial fluid flows. The principle for a vortex flow meter has also attracted a lot of attention [4–6]. A vortex shedding after a square rod for transitional flow in two dimensions is also simulated by means of the T4/C3 finite element formulation.

2. GOVERNING EQUATIONS AND COMPUTATIONAL METHOD

The Navier–Stokes equations in two dimensions for incompressible flow are represented by

$$\frac{\partial u}{\partial t}+u\frac{\partial u}{\partial x}+v\frac{\partial u}{\partial y}=\frac{1}{\rho}F_x-\frac{1}{\rho}\frac{\partial p}{\partial x}+v\left(\frac{\partial^2 u}{\partial x^2}+\frac{\partial^2 u}{\partial y^2}\right) \tag{1}$$

$$\frac{\partial v}{\partial t}+u\frac{\partial v}{\partial x}+v\frac{\partial v}{\partial y}=\frac{1}{\rho}F_y-\frac{1}{\rho}\frac{\partial p}{\partial y}+v\left(\frac{\partial^2 v}{\partial x^2}+\frac{\partial^2 v}{\partial y^2}\right) \tag{2}$$

The principle of mass conservation must not be violated, and is represented by

$$\frac{\partial u}{\partial u}+\frac{\partial v}{\partial y}=0 \tag{3}$$

in which u and v are the velocities in the x- and y-directions respectively, p is the pressure, F_x and F_y are the body forces in the x- and y-directions respectively, ρ is the density, and v denotes the kinematic viscosity.

The related conceptual configurations for 4- and 3-node shape functions respectively are shown in Figure 1, and the T4/C3 element shape functions for velocity and pressure are represented by Equations (4) and (5)

$$\begin{bmatrix} N_1 \\ N_2 \\ N_3 \\ N_4 \end{bmatrix} = \begin{bmatrix} 1 & 0 & 0 & -1/3 \\ 0 & 1 & 0 & -1/3 \\ 0 & 0 & 1 & -1/3 \\ 0 & 0 & 0 & 1 \end{bmatrix} \begin{bmatrix} L_1 \\ L_2 \\ L_3 \\ 27L_1L_2L_3 \end{bmatrix} \tag{4}$$

$$\begin{bmatrix} M_1 \\ M_2 \\ M_3 \end{bmatrix} = \begin{bmatrix} 1 & 0 & 0 \\ 0 & 1 & 0 \\ 0 & 0 & 1 \end{bmatrix} \begin{bmatrix} L_1 \\ L_2 \\ L_3 \end{bmatrix} \tag{5}$$

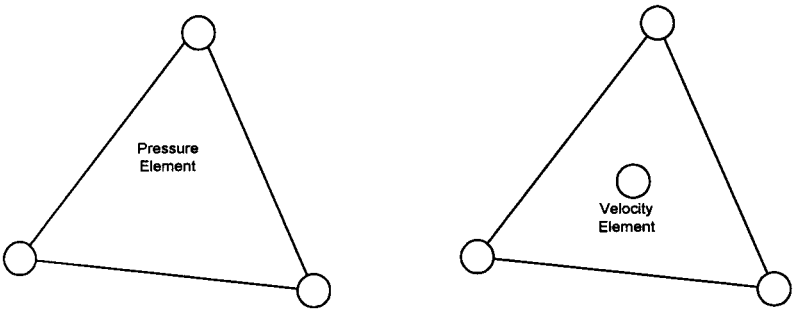

Figure 1. Elements for pressure and velocity.

in which N_i $(i = 1, 2, 3, 4)$ is the shape function for velocity, M_i is the shape function for pressure, and L_i is defined by

$$L_i = a_i + b_i x + c_i y$$

where

$$a_i = \frac{1}{2\triangle}(x_j y_k - x_k y_i)$$

$$b_i = \frac{1}{2\triangle}(y_j - y_k)$$

$$c_i = \frac{1}{2\triangle}(x_k - x_j)$$

$$i = 1, 2, 3; \quad j = 1, 2, 3; \quad k = 1, 2, 3, \quad i \neq j \neq k$$

and where $\triangle$ represents the area of triangular element.

Following the usual Galerkin procedure, Equations (1)–(3), incorporating the shape functions defined by Equations (4) and (5), become time-dependent discretized forms, as Equations (6)–(8)

$$\begin{aligned}
&\sum_1^{ne} \int_{A^e} \left\{ N_i \left[\sum_1^4 N_j \frac{\partial u_j}{\partial t} + \sum_1^4 N_k u_k \sum_1^4 \frac{\partial N_j}{\partial x} u_j + \sum_1^4 N_k v_k \sum_1^4 \frac{\partial N_j}{\partial y} u_j \right] \right. \\
&\left. + \frac{\partial N_i}{\partial x} \left(2v \sum_1^4 \frac{\partial N_j}{\partial x} u_j - \frac{1}{\rho} \sum_1^3 M_l p_l \right) + v \frac{\partial N_i}{\partial y} \left(\sum_1^4 \frac{\partial N_j}{\partial y} u_j + \sum_1^4 \frac{\partial N_j}{\partial x} v_j \right) \right\} \mathrm{d}A^e \\
&= \int_\Gamma \left\{ N_i \frac{1}{\rho} \left(- \sum_1^3 M_l p_l + 2\mu \sum_1^4 \frac{\partial N_j}{\partial x} u_j \right) l_x + v N_i \left(\sum_1^4 \frac{\partial N_j}{\partial x} v_j + \sum_1^4 \frac{\partial N_j}{\partial y} u_j) \right) l_y \right\} \mathrm{d}\Gamma \\
&\quad + \sum_1^{ne} \int_{A^e} N_i F_x \, \mathrm{d}A^e
\end{aligned} \tag{6}$$

$$\sum_{1}^{ne}\int_{A^e}\left\{N_i\left[\sum_{1}^{4}N_j\frac{\partial v_j}{\partial t}+\sum_{1}^{4}N_k u_k\sum_{1}^{4}\frac{\partial N_j}{\partial x}v_j+\sum_{1}^{4}N_k v_k\sum_{1}^{4}\frac{\partial N_j}{\partial y}v_j\right]\right.$$
$$\left.+\frac{\partial N_i}{\partial y}\left(2\nu\sum_{1}^{4}\frac{\partial N_j}{\partial y}v_j-\frac{1}{\rho}\sum_{1}^{3}M_l p_l\right)+\nu\frac{\partial N_i}{\partial x}\left(\sum_{1}^{4}\frac{\partial N_j}{\partial y}u_j+\sum_{1}^{4}\frac{\partial N_j}{\partial x}v_j\right)\right\}\mathrm{d}A^e$$
$$=\int_{\Gamma}\left\{N_i\frac{1}{\rho}\left(-\sum_{1}^{3}M_l p_l+2\mu\sum_{1}^{4}\frac{\partial N_j}{\partial y}v_j\right)l_y+\nu N_i\left(\sum_{1}^{4}\frac{\partial N_j}{\partial x}v_j+\sum_{1}^{4}\frac{\partial N_j}{\partial y}u_j\right)l_y\right\}\mathrm{d}\Gamma$$
$$+\sum_{1}^{ne}\int_{A^e}N_i F_y\,\mathrm{d}A^e \tag{7}$$

$$\sum_{1}^{ne}\int_{A^e}M_i\left(\sum_{1}^{4}\frac{\partial N_j}{\partial x}v_j+\sum_{1}^{4}\frac{\partial N_j}{\partial y}v_j\right)\mathrm{d}A^e=0 \tag{8}$$

The resulting equations can be written in matrix form

$$\mathbf{M}\dot{\gamma}+\mathbf{A}\lambda=\mathbf{F} \tag{9}$$

in which $\lambda=\{\lambda_i\}$, $\dot{\gamma}=\{\dot{\gamma}_i\}$, $M=[m_{ij}]$, and $A=[a_{ij}]$. Their forms are listed below

$$\lambda_i=\begin{Bmatrix}u_i\\p_i\\v_i\end{Bmatrix},\qquad \dot{\gamma}_i=\begin{Bmatrix}\dfrac{\partial u_j}{\partial t}\\[2mm]\dfrac{\partial v_j}{\partial t}\end{Bmatrix},\qquad m_{ij}=\sum_{1}^{ne}\int_{A^e}\begin{bmatrix}N_iN_j&0&0\\0&0&0\\0&0&N_iN_j\end{bmatrix}\mathrm{d}A^e$$

$$a_{ij}=\sum_{1}^{ne}\int_{A^e}\begin{bmatrix}C_{11}&C_{12}&C_{13}\\C_{21}&C_{22}&C_{23}\\C_{31}&C_{32}&C_{33}\end{bmatrix}\mathrm{d}A^e$$

where

$$C_{11}=N_iN_k\tilde{u}_k\frac{\partial N_j}{\partial x}+N_iN_k\tilde{v}_k\frac{\partial N_j}{\partial y}+\nu\left(2\frac{\partial N_i}{\partial x}\frac{\partial N_j}{\partial x}+\frac{\partial N_i}{\partial y}\frac{\partial N_j}{\partial y}\right)$$

$$C_{12}=-M_l\frac{1}{\rho}\frac{\partial N_i}{\partial x},\qquad C_{13}=\nu\frac{\partial N_j}{\partial y}\frac{\partial N_j}{\partial x},\qquad C_{21}=M_l\frac{\partial N_j}{\partial x},\qquad C_{22}=0$$

$$C_{23}=M_l\frac{\partial N_j}{\partial y},\qquad C_{31}=\nu\frac{\partial N_i}{\partial x}\frac{\partial N_j}{\partial y},\qquad C_{32}=-M_l\frac{1}{\rho}\frac{\partial N_i}{\partial y}$$

$$C_{33} = N_i N_k \tilde{u}_k \frac{\partial N_j}{\partial x} + N_i N_k \tilde{v}_k \frac{\partial N_j}{\partial y} + \nu\left(\frac{\partial N_i}{\partial x}\frac{\partial N_j}{\partial x} + 2\frac{\partial N_i}{\partial y}\frac{\partial N_j}{\partial y}\right)$$

and $\mathbf{F} = [F_i]$ is called a load vector or forcing function. The components of the forcing function are given by

$$F_i = \sum_1^{ne} \int_{A^e} \begin{Bmatrix} f_{i,1} \\ f_{i,2} \\ f_{i,3} \end{Bmatrix} \mathrm{d}A^e + \sum_1^{ne} \int_{\Gamma^e} \begin{Bmatrix} b_{i,1} \\ b_{i,2} \\ b_{i,3} \end{Bmatrix} \mathrm{d}\Gamma$$

where

$$f_{i,1} = N_i \frac{F_x}{\rho}, \qquad f_{i,2} = 0, \qquad f_{i,3} = N_i \frac{F_y}{\rho}$$

$$b_{i,1} = \frac{N_i f_x}{\rho}, \qquad b_{i,2} = 0, \qquad b_{i,3} = \frac{N_i f_y}{\rho}$$

and F_x and F_y are directional body forces and are represented by

$$f_x = l_x\left(-p + 2\mu\frac{\partial u}{\partial x}\right) + l_y\mu\left(\frac{\partial u}{\partial y} + \frac{\partial v}{\partial x}\right), \qquad f_y = l_y\left(-p + 2\mu\frac{\partial v}{\partial y}\right) + l_x\mu\left(\frac{\partial u}{\partial y} + \frac{\partial v}{\partial x}\right)$$

Hence f_x and f_y can be immediately identified as normal and tangential traction components and l_x and l_y are direction cosines of the outward normal to boundary Γ^e.

It should be noted that the time derivatives for velocities can be expanded in finite difference form as

$$\frac{\partial u}{\partial t} = \frac{u^{[k+1]} - u^{[k]}}{\Delta t} \tag{10}$$

$$\frac{\partial v}{\partial t} = \frac{v^{[k+1]} - v^{[k]}}{\Delta t} \tag{11}$$

$$u = \theta u^{[k+1]} + (1-\theta)u^{[k]} \tag{12}$$

$$v = \theta v^{[k+1]} + (1-\theta)v^{[k]} \tag{13}$$

in which θ denotes the factor of implicit scheme [7] and $\theta > 0.5$ stands for unconditionally stable [7]. The steady state, incompressible governing equations can also be treated in a similar way. The frontal solution [8] and Picard iteration procedure [1] were employed to solve these discretized equations. It should be pointed out that this formulation did not use the upwinding technique to suppress the wiggles, while the local Reynolds number ($Re = (u_c \times l_c)/\nu$, in which

u_c and l_c are local characteristic velocity and length respectively) was increased. Convergence is defined by the specification that the maximum relative error is less than 0.01 and this criterion is acceptable when numerical results are compared with experimental data or other simulations [9–14].

3. NUMERICAL RESULTS

3.1. Driven cavity flow

The flow system considered is a lid-driven cavity shown (Figure 2). The three non-slip boundary conditions and a slip boundary condition with $u_0 = 1$ for the domain of interest are also shown in Figure 2. For the T4/C3 element, only one boundary condition for pressure was adopted to avoid the numerical singularity. In this system, the Reynolds number is expressed as

$$Re = \frac{u_0 \times l}{v}$$

in which u_0 is the velocity at the top side and l is length of the cavity.

Two different grids are shown in Figures 3 and 4 for the coarse mesh and the fine mesh respectively. The coarse mesh contains 225 nodal points and 392 elements. The fine mesh contains 1000 nodal points and 1874 elements. For a Reynolds number equal to 1.0E − 5, the center of the eddy is approximately located at $x = 0.5$ and $y = 0.75$. The results of $Re =$ 1.0E − 5 and of $Re = 400$, as well as a comparison with Burggraf [9], are shown in Figure 5. The corresponding streamline plots are shown in Figures 6 and 7 respectively, for illustrative purposes. It is shown that the results of $Re = 400$ from the fine mesh are clearly superior to those from the coarse mesh. For $Re = 1000$, the simulation with the coarse mesh failed to converge because of no upwinding technique involved. However, Figure 8 depicts the

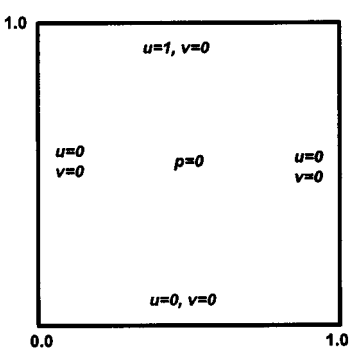

Figure 2. Geometry and boundary conditions for driven cavity flow.

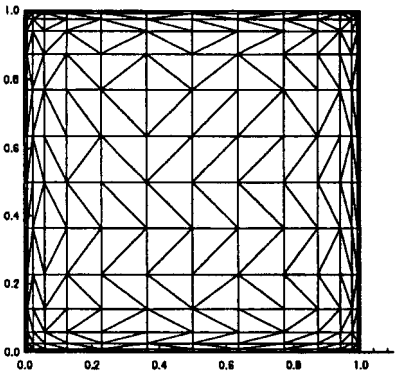

Figure 3. Coarse mesh for driven cavity flow.

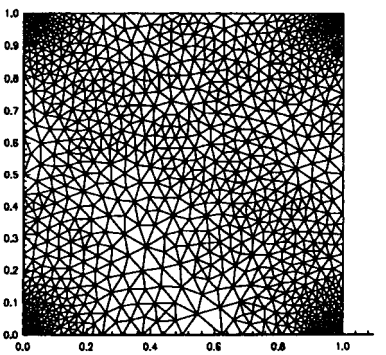

Figure 4. Fine mesh for driven cavity flow.

streamline plot of the simulation results for $Re = 1000$ from the fine mesh and the results are identical to Ren and Utness [10]. All calculations were performed on a Pentium II 200, and the program was written in Fortran.

The comparisons between the Q8/C4 and the T4/C3 finite elements for driven cavity flow simulation in different structural meshes are listed in Table I. It demonstrates that the T4/C3 element is more efficient than the higher-order elements in terms of the computational speed.

3.2. Flow over a backward-facing step

The flow over a backward-facing step frequently occurs in many chemical engineering processes. The simulated geometry considered and boundary conditions are depicted in Figure 9 The inlet boundary condition was a fully developed Poiseuille parabolic velocity profile, and zero pressure condition was adopted at the outlet. In this system, the Reynolds number is defined as

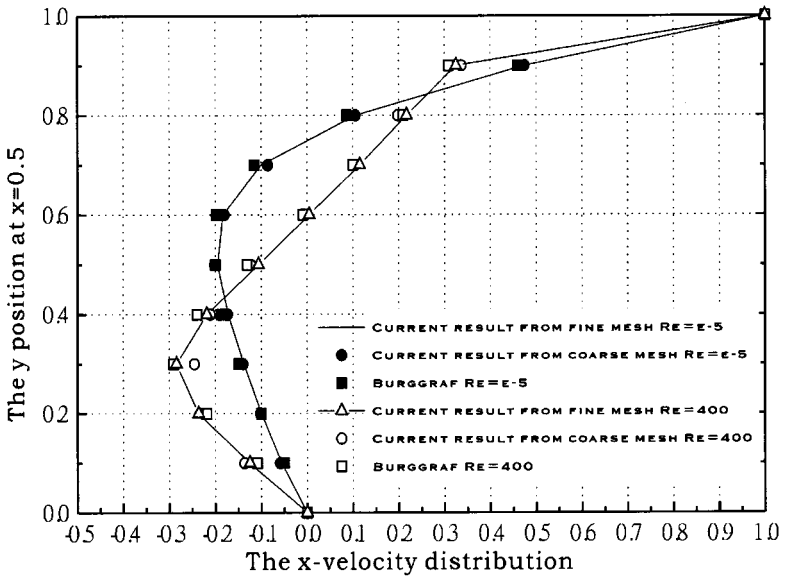

Figure 5. Result compared with Burggraf [9].

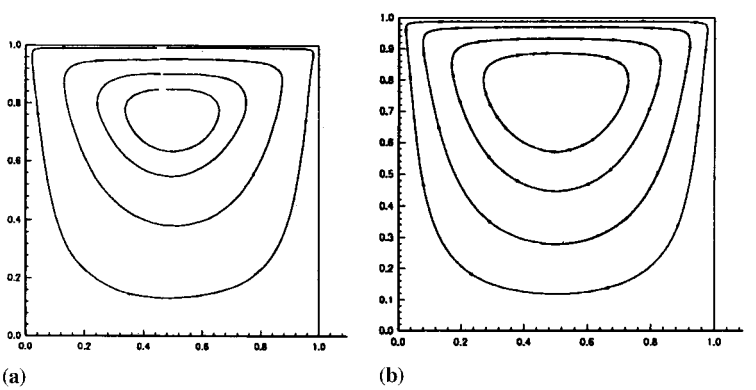

Figure 6. Streamline plotting for $Re = 0.00001$; (a) coarse mesh, (b) fine mesh.

$$Re = \frac{u_0 \times l}{v}$$

where u_0 is the mean inlet velocity and l is the height of the backward step.

Again, two different sizes of grid were used to show the grid independence of the solution. Coarse and fine meshes are shown in Figures 10 and 11 respectively, as well as the

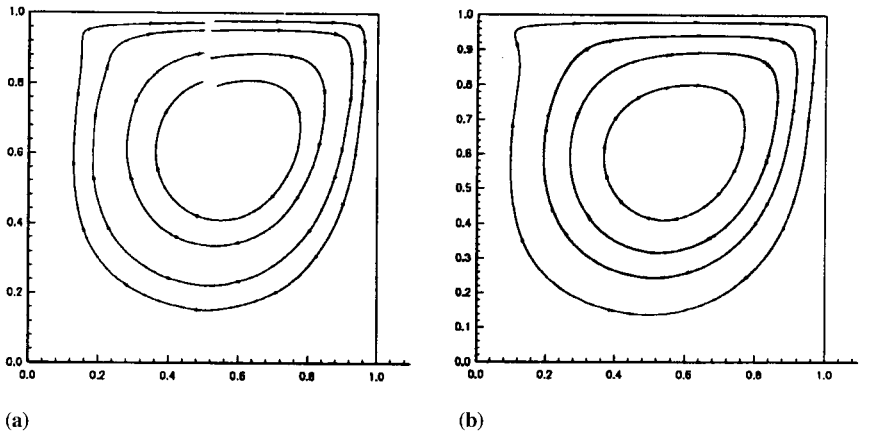

Figure 7. Streamline plotting for $Re = 400$; (a) coarse mesh, (b) fine mesh.

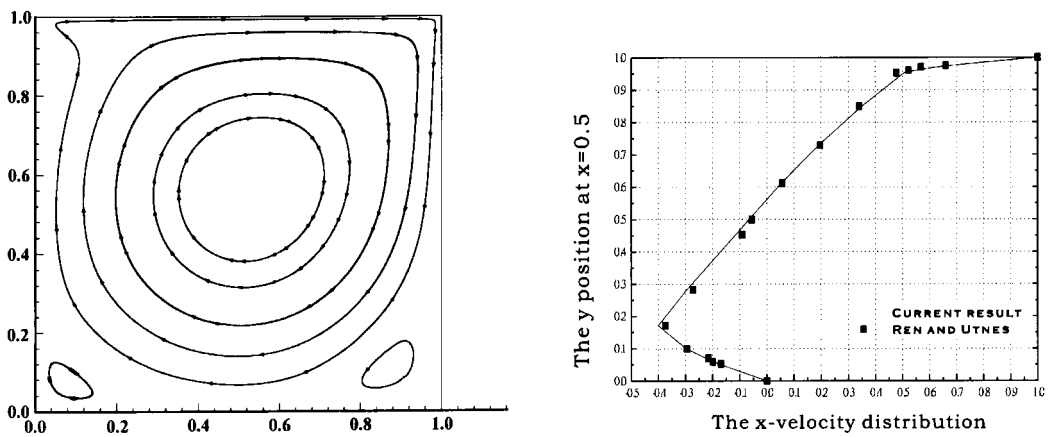

Figure 8. Results for $Re = 1000$; (a) streamline plot, (b) comparison with Ren and Utnes [10].

Table I. Comparisons between the Q8/C4 element and the T4/C3 element.

Element type	Number of elements	Number of nodes	Maximum frontal width	CPU time (s)	Number of iterations	Number of equations
Q8/C4	100	341	65	81.85	12	803
T4/C3	128	209	35	15.70	9	499
T4/C3	200	321	41	39.33	11	763

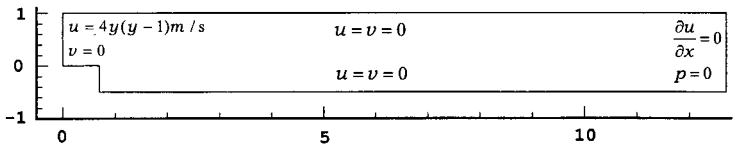

Figure 9. Geometry and boundary conditions for backward-facing step.

Figure 10. Coarse mesh for backward-facing step.

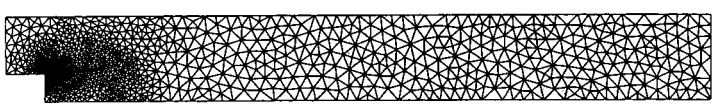

Figure 11. Fine mesh for backward-facing step.

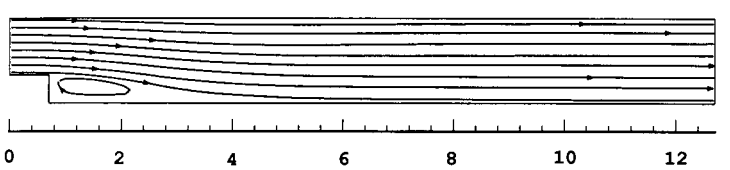

Figure 12. Streamline plotting for $Re = 73$ in coarse mesh.

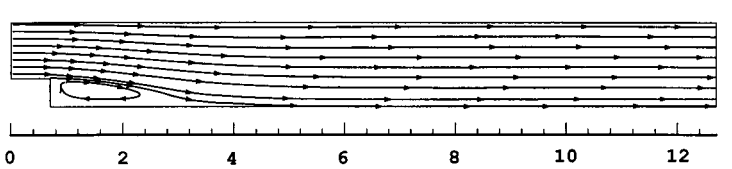

Figure 13. Streamline plotting for $Re = 73$ in fine mesh.

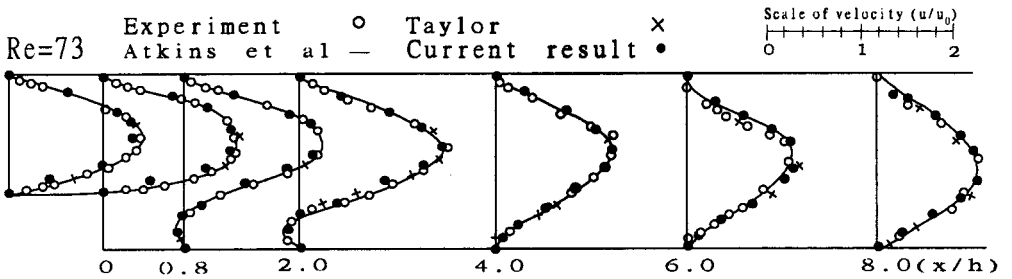

Figure 14. Comparisons with other results.

corresponding streamlines of $Re = 73$ (illustrated in Figures 12 and 13). Even the results from the coarse mesh show a very good agreement with the results of Taylor [1], the experimental data [11], or Atkins *et al.* [12], as illustrated in Figure 14.

3.3. Confined surface rib flow

This case could be found in many practical applications, such as the inserted fins with air or liquid flowing through them and are often used for heat transfer enhancement. The simulated geometry considered and the boundary conditions are indicated in Figure 15. The inlet velocity is uniform and the outlet condition is a zero pressure condition. In this system, the Reynolds number is defined as

$$Re = \frac{u_0 \times l}{v}$$

where u_0 is the inlet velocity and l is length of the rib.

The mesh used is shown in Figure 16 and the corresponding streamline profile of $Re = 200$ is shown in Figure 17. The recirculation zone length, which is the ratio of vortex length to rib length, is approximately equal to 7.00. The similar result obtained by Roache and Mueller [13] and Leone and Gresho [14] was approximately 6.75. The relative difference is 3.57 per cent.

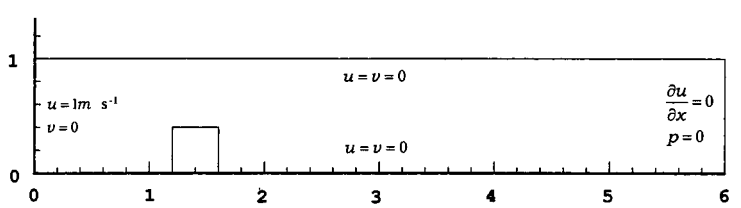

Figure 15. Geometry and boundary conditions for flow passing surface rib.

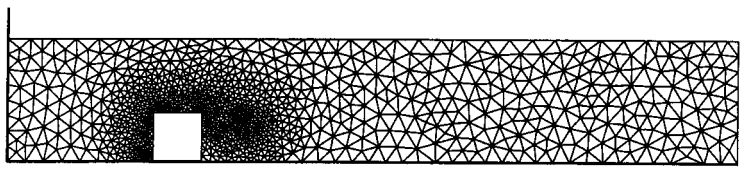

Figure 16. Mesh for surface rib flow.

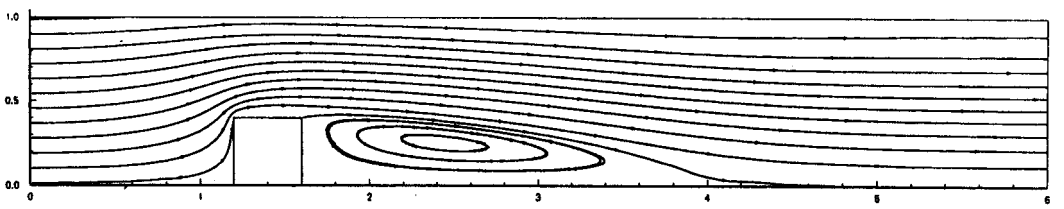

Figure 17. Streamline plotting for surface rib flow ($Re = 200$).

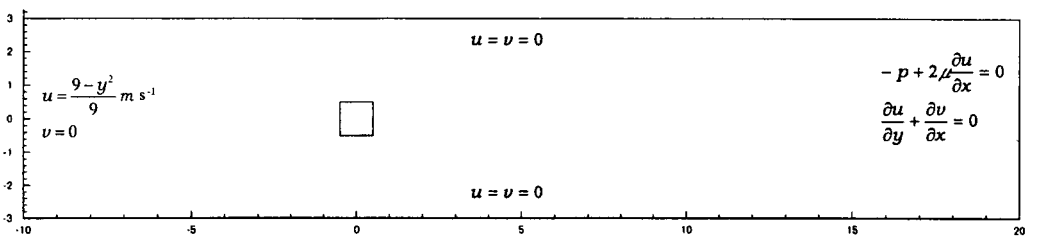

Figure 18. Geometry and boundary conditions for vortex shedding after a square.

3.4. Two-dimensional vortex shedding simulation

The complete geometry and boundary conditions are shown in Figure 18. It should be noted that the zero traction boundary condition was prescribed at the outlet.

The mesh profile is shown in Figure 19. Two non-dimensional groups are defined as

$$Re = \frac{u_0 \times l}{v}$$

and

$$St = \frac{f \times l}{u_0}$$

in which u_0 is the inlet velocity at the centerline, l is the length of the square, and f is the frequency of vortex shedding.

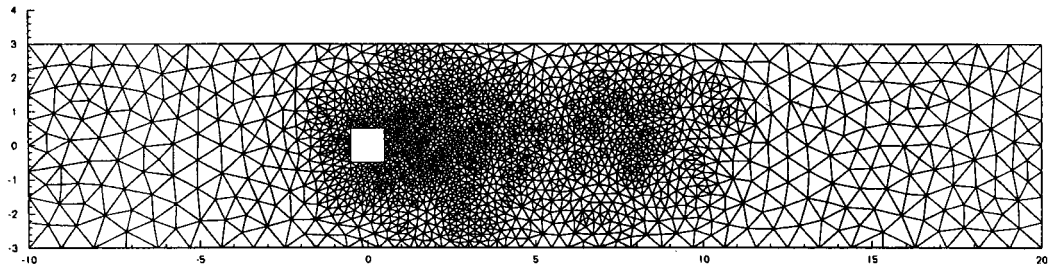

Figure 19. Mesh for vortex shedding.

For comparison purposes, a flow field of $Re = 250$ was simulated. In order to see the vortex oscillation, local points (3, 0), (5, 0), and (7, 0) were chosen and the histories of (u, p, v) for these points are shown in Figures 20–28. The vibrated pressure distributions are also shown in Figures 29 and 30. In this case, the Strouhal number (St), the frequency of the oscillation in the y-direction, is approximately 0.14. This shows a good agreement with the result of Davis *et al.* [4].

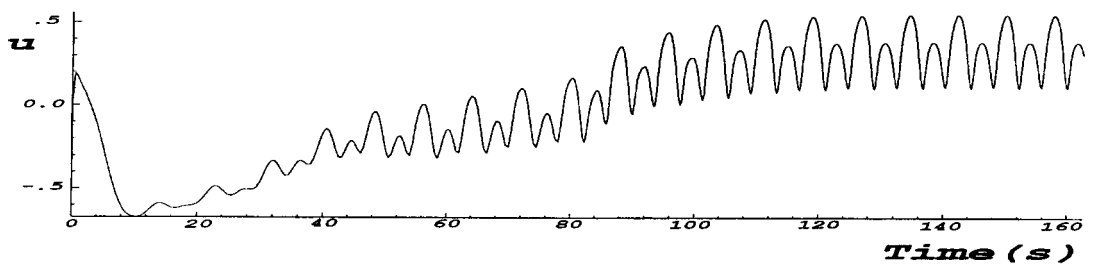

Figure 20. u history for point (3, 0).

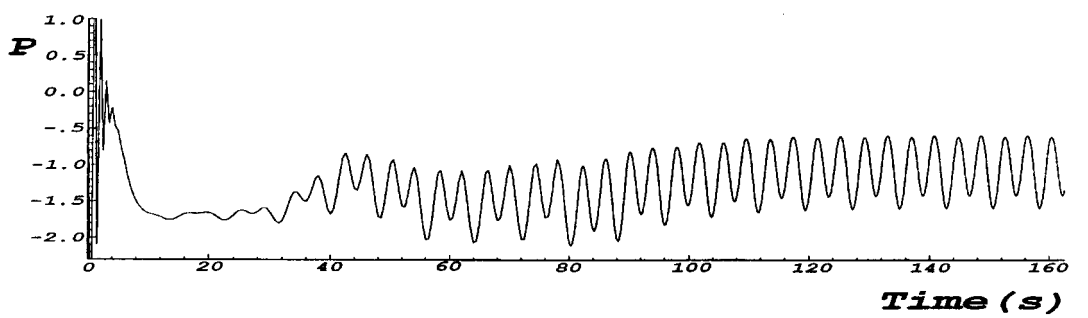

Figure 21. p history for point (3, 0).

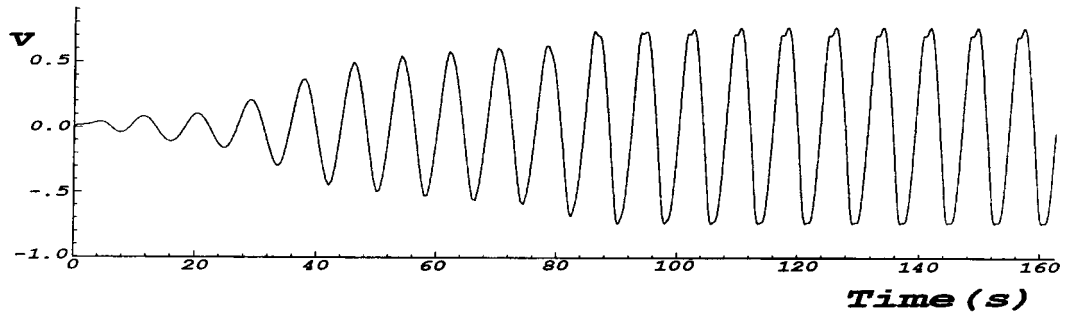

Figure 22. v history for point (3, 0).

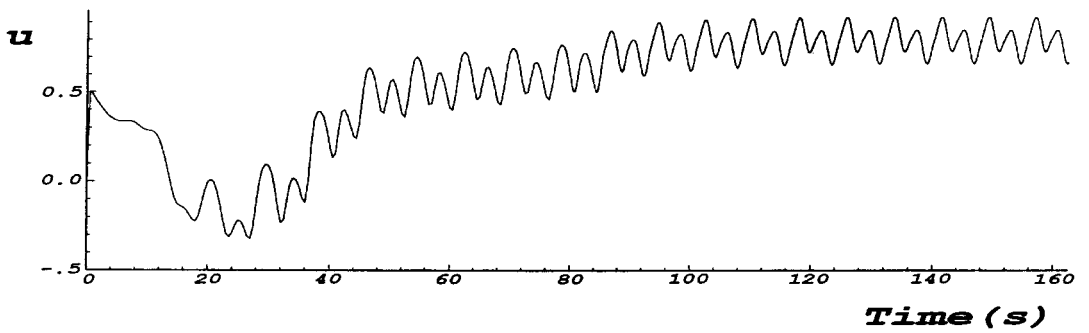

Figure 23. u history for point (5, 0).

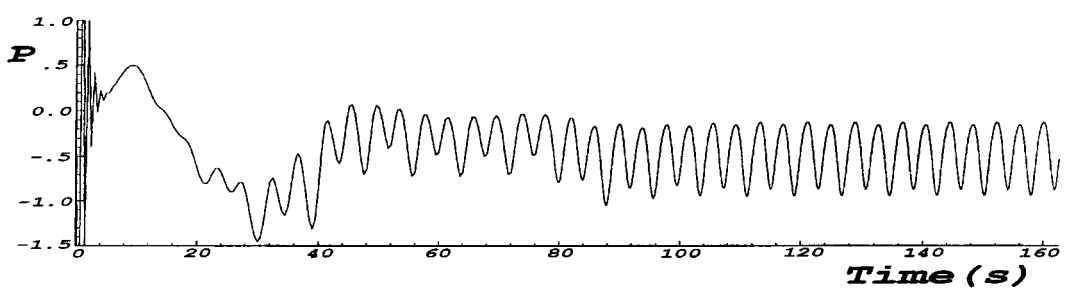

Figure 24. p history for point (5, 0).

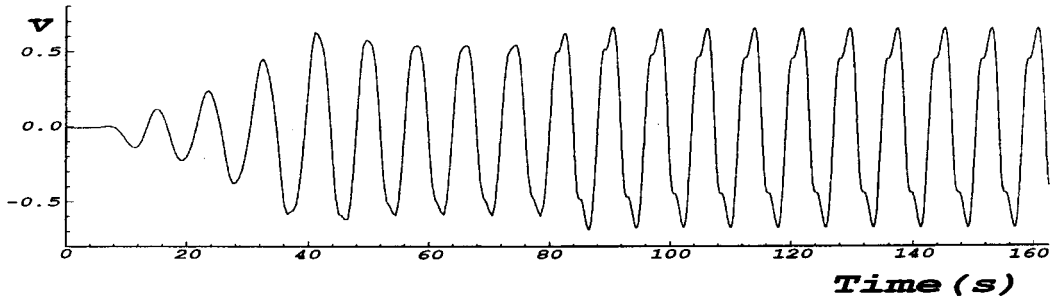

Figure 25. v history for point (5, 0).

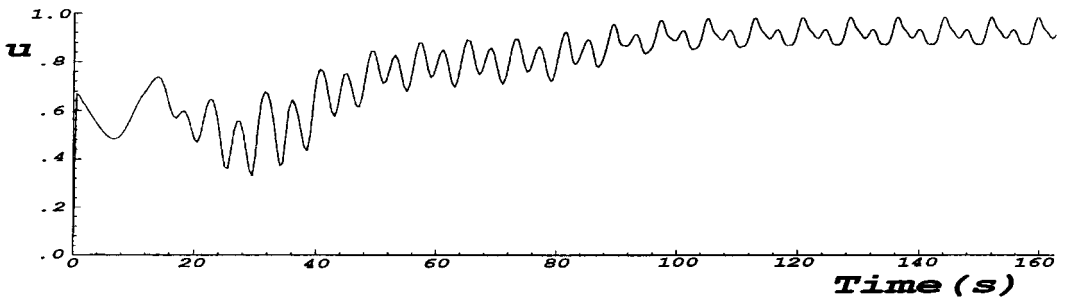

Figure 26. u history for point (7, 0).

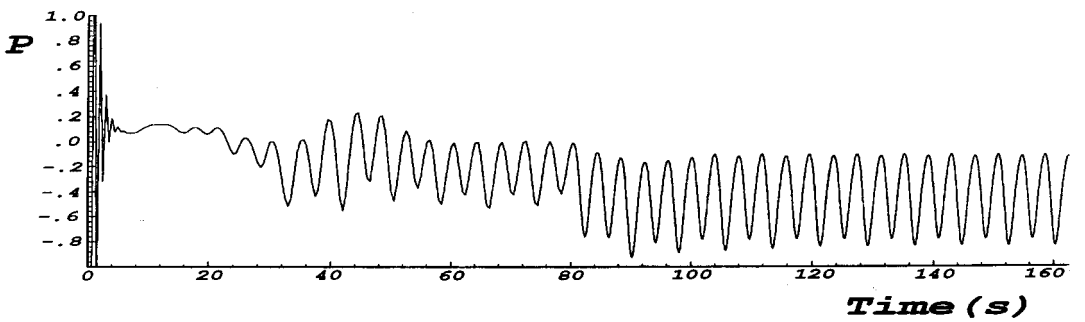

Figure 27. p history for point (7, 0).

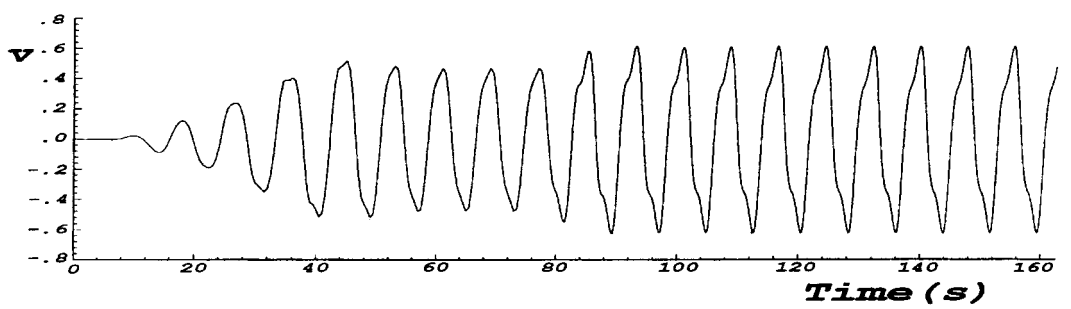

Figure 28. v history for point (7, 0).

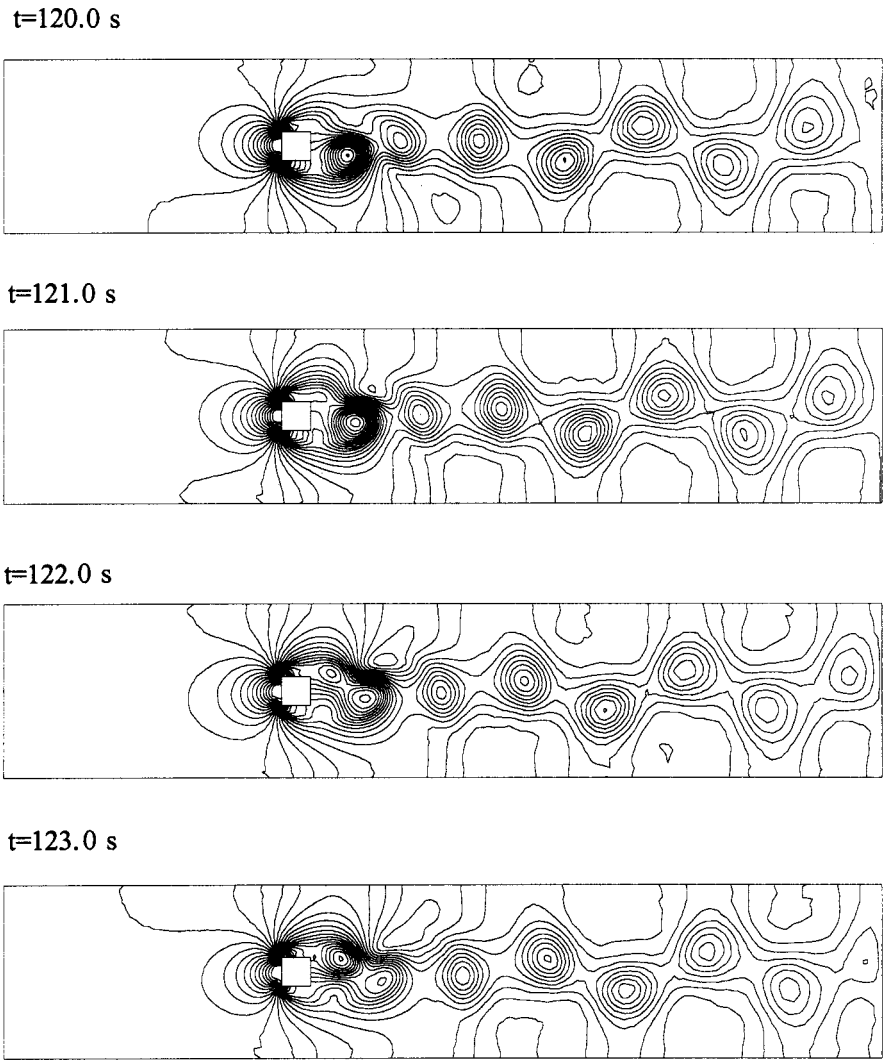

Figure 29. Pressure variation for vortex shedding ($Re = 250$).

4. CONCLUSIONS

The T4/C3 element fluid flow simulations for both steady state and transitional vortex shedding in two dimensions are carried out in this paper, Because of its simplicity and the exact surface integration, as well as smaller frontal widths [8] compared with those of higher-order elements, the intense calculations can be substantially reduced in every iteration while advancing the time step. It should be pointed out again that this formulation does not use the upwinding scheme to stabilize or speed up the numerical solutions.

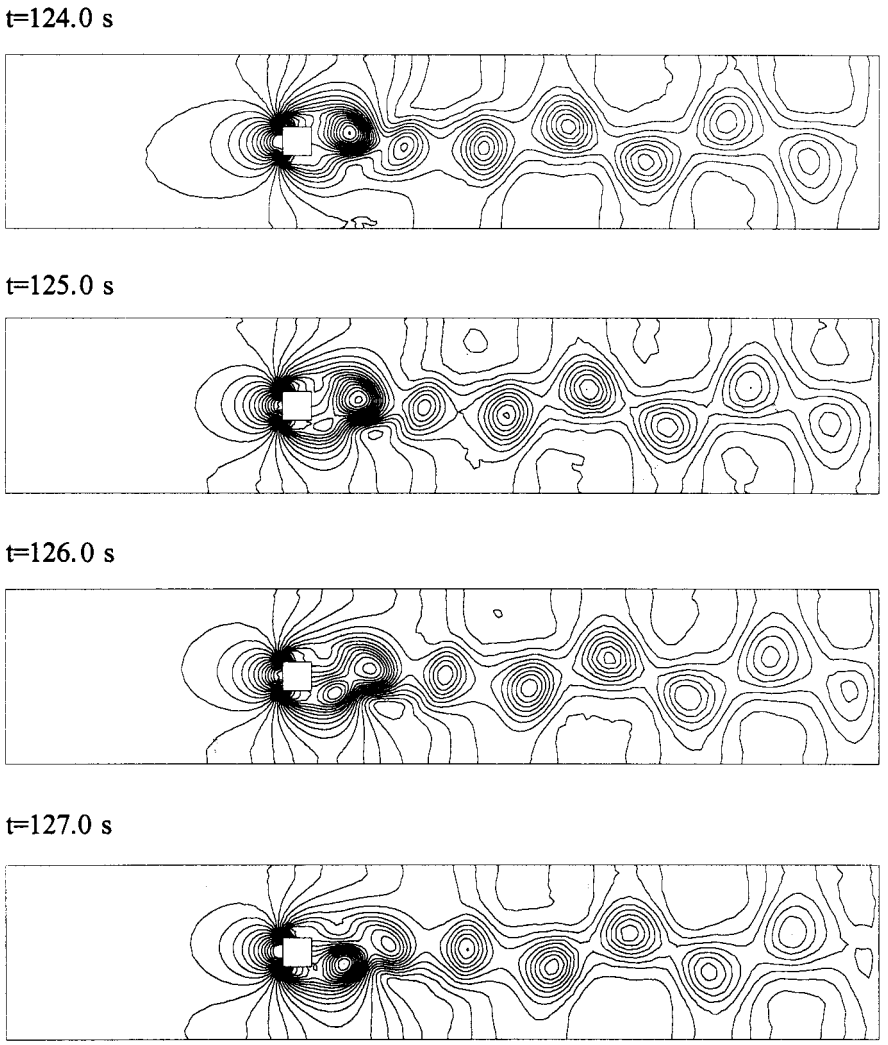

Figure 30. Pressure variation for vortex shedding ($Re = 250$).

APPENDIX A. NOMENCLATURE

A advection–diffusion matrix
A^e domain of element
C continuous shape function
F load vector
F_x body force aligned in the x co-ordinate direction

F_y body force aligned in the y co-ordinate direction
f frequency of the vortex shedding
l_c characteristic length
l_x x-direction cosine of the outward normal to boundary
l_y y-direction cosine of the outward normal to boundary
$\mathbf{M}$ mass matrix
M_i shape function for three nodes in triangular elements
N_i shape function for four nodes in triangular elements
ne number of elements
p pressure v
Re Reynolds number
Q quadrangular element
St Strouhal number
T triangular element
u x velocity component
u_0 characteristic velocity
v y velocity component
$\triangle$ area of triangular element

Greek letters
μ viscosity
v kinematic viscosity
ρ density
θ factor of implicit scheme
Γ boundary

Superscript
$[k]$ kth time step

Subscript
i ith node in element

REFERENCES

1. Taylor C, Hughes TG. *Finite Element Programming of the Navier–Stokes Equations*. Pineridge Press: Swansea, 1981.
2. Huyakorn PS, Taylor C, Lee RL, Gresho PM. A comparison of various mixed-interpolation finite elements in the velocity-pressure formulation of Navier–Stokes equations. *Computers in Fluids* 1978; **6**: 25–35.
3. Fortin M, Fortin A. Newer and newer elements for incompressible flow. In *Finite Element in Fluid*, vol. 6, Gallagher RH, *et al.* (eds). Wiley: New York, 1985; 171–187.
4. Davis RW, Moore EF, Purtell LP. A numerical–experimental study of confined flow around rectangular cylinders. *Physics of Fluids* 1984; **27**(1): 46–59.
5. Suzuki H, Inoue Y, Nishimura T, Fukutani K, Suzuki K. Unsteady flow in a channel obstructed by a square rod (crisscross motion of vortex). *International Journal for Heat and Fluid Flow* 1993; **14**(1): 2–9.

6. Li G, Humphrey JAC. Numerical modelling of confined flow past a cylinder of square cross-section at various orientations. *International Journal for Numerical Methods in Fluids* 1995; **20**: 1215–1236.
7. Zienkiewicz OC, Taylor RL. *The Finite Element Method* (4th edn), vol. 2. McGraw-Hill: Berkshire, 1989.
8. Irons MB. A frontal solution program for finite element analysis. *International Journal for Numerical Methods in Engineering* 1970; **2**: 5–32.
9. Burggraf F. Analytical and numerical studies of the structure of steady separated flowed. *Journal of Fluid Mechanics* 1966; **24**: 113–151.
10. Ren G, Utnes T. A finite element solution of the time-dependent incompressible Navier–Stokes equations using a modified velocity correction method. *International Journal for Numerical Methods in Fluids* 1993; **17**: 349–364.
11. Denham MK, Patrick MA. Laminar flow over a downstream facing step in a two-dimensional flow channel. *Transactions of the Institute of Chemical Engineers* 1974; **52**(4): 361–367.
12. Atkins DJ, Maskall SJ, Patrick MA. A numerical prediction of separated flow. *International Journal for Numerical Methods in Engineering* 1980; **15**: 129–144.
13. Roache P, Mueller T. Numerical solutions of laminar separated flows. *AIAA Journal* 1970; **8**(3): 530–538.
14. Leone LM, Gresho PM. Finite element simulation of steady, two dimensional, viscous incompressible flow over a step. *Journal of Computational Physics* 1981; **41**: 167–191.

